Defect-Rich Crystalline SnO2 Immobilized on Graphene Nanosheets with Enhanced Cycle Performance for Li Ion Batteries

Dongniu Wang,[†,‡] Xifei Li,[†] Jiajun Wang,[†] Jinli Yang,[†] Dongsheng Geng,[†] Ruying Li,[†] Mei Cai,[§] Tsun-Kong Sham,*,[‡] and Xueliang Sun*,[†]

[†]Department of Mechanical and Materials Engineering, University of Western Ontario, London, Ontario N6A 5B7, Canada
[‡]Department of Chemistry, University of Western Ontario, London, Ontario N6A 5B7, Canada
[§]General Motors R&D Center, Warren, Michigan 48090-9055, United States

Ⓢ *Supporting Information*

ABSTRACT: A one-step microwave-assisted hydrothermal method (MAHM) has been developed to synthesize SnO2/graphene composites. It is shown that fine SnO2 nanoparticles with an average size of 3.5 nm can be homogeneously deposited on graphene nanosheets (GNSs) using this technique. The electronic structure as revealed from X-ray absorption near edge structure (XANES) shows that the SnO2 nanoparticles are abundant in surface defects with oxygen vacancies, which facilitate the immobilization of SnO2 onto GNSs by electronic interaction. Carbon K edge XANES provide direct evidence of strong interaction between SnO2 and GNSs. The SnO2/graphene nanocomposites deliver a superior reversible capacity of 635 mAh g^{-1} after 100 cycles and display excellent rate performance. All these desirable features strongly indicate that SnO2/graphene composite is a promising anode material in high-performance lithium ion batteries.
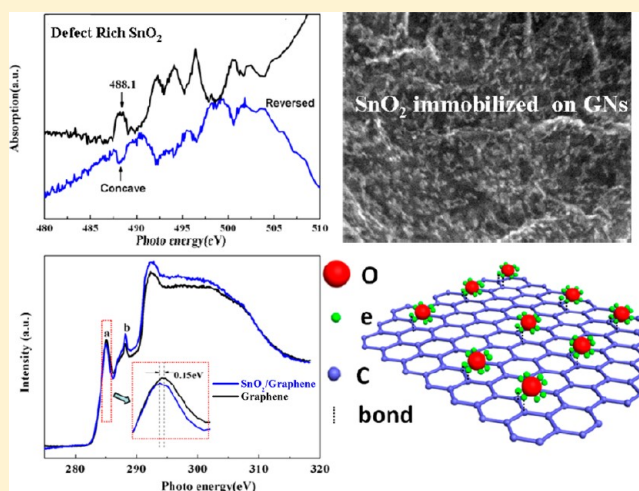
1. INTRODUCTION

Lithium ion battery (LIB) is currently the dominant power source for portable electronic devices due to its high energy density, working voltage, electromotive force, and light weight. Recent years have witnessed the intensive research effort that has been aimed at developing high capacity LIB electrodes with good stability for application in electrical/hybrid-electrical vehicles. Since the commercial graphite anode has a limited specific capacity of 372 mAh g^{-1}, much research attempts are focused on exploring graphite alternatives with high energy capacities. SnO2 is considered as one of the most promising substitutes because of its high lithium storage capability up to 782 mAh g^{-1}, more than twice as that of graphite.[1−6] However, the major drawback hampering its industrial application is the poor cycling performance, which is caused by serious aggregation and considerable volume change upon cycling.[7,8]

One effective strategy commonly used to address these problems is to disperse SnO2 nanocrystals on ductile carbonaceous support as a buffer matrix to maintain the electrode integrity during the charge/discharge process.[9−11] For example, improved battery performance has been achieved by loading SnO2 on graphite or carbon nanotubes, etc.[10,12,13] Among all carbonaceous materials, graphene nanosheets (GNSs) has been regarded as a good matrix for SnO2 anode since it has ultrathin graphitic layers, excellent electronic conductivity, high surface areas (2600 m² g^{-1}), good mechanical properties, and chemical stabilities.[14−16] Recent reports showed that hybrid SnO2/GNSs nanocomposites exhibited enhanced cycle performance.[4,17,18] Whereas, in order to facilitate the hybridization between SnO2 and GNSs, additional reagents such as urea have to be applied in the solution, leading to complicated synthesis procedures and increased cost. In addition, it is often difficult to control the uniform deposition of metal oxide on GNSs since the whole GNSs is not homogeneously functionalized at its widespread surface.[4,18] In situ chemical synthesis of SnO2/graphene composites requires post thermal treatment, resulting in time-consuming and complicated synthesis methodology.[19] As previously reported by our group,[17] we designed the SnO2/graphene composites via atomic layer deposition, demonstrating that this hybrid structure favors the increase of the electrochemical performance. Paek et al.[4] and Zhang et al.[20] synthesized the SnO2/graphene composites and found improved cycling performance compared with that of bare

SnO_2; Yao et al.[19] and Lian et al.[21] prepared the SnO_2/graphene hybrids by an in situ chemical synthesis approach. The composites exhibit both high reversible specific capacity and excellent rate capability. Generally, enhanced performances are attributed to synergic effect of the hybrids. Despite the excellent electrochemical performances, up to now, little research has been focused on studying the electronic structure, chemical environment, chemical bonding, and charge transfer between SnO_2 and GNSs behind that. Thus, investigation of how SnO_2 nanoparticles are immobilized or anchored on the GNSs is very relevant for the formation of resultant nanocomposites achieving desired performance.

Herein, we report a facile, simple and efficient microwave-assisted hydrothermal method (MWHM) to synthesize hybrid SnO_2/graphene nanocomposites without employing surfactants or templates (Scheme 1) and then investigate the interaction

Scheme 1. Illustration of Microwave-Assisted Hydrothermal System and Synthesis Process of SnO_2/Graphene Nanocomposites
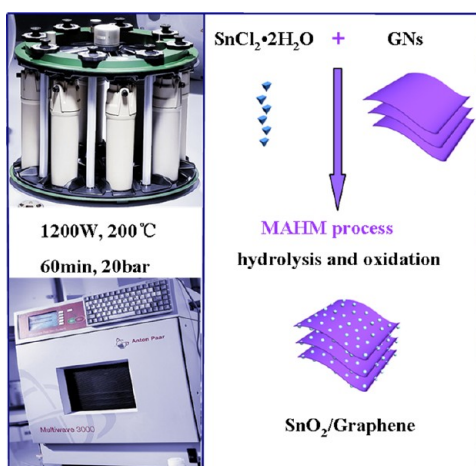
between SnO_2 and GNSs using XANES. It is found that the rich surface defects of uniformly dispersed SnO_2 nanoparticles and the presence of oxygen based defects on the GNSs facilitate the immobilization onto GNSs and that such hybrid composites deliver a high reversible capacity of 635 mAh g^{-1} after 100 cycles and an excellent rate capability.

2. EXPERIMENTAL SECTION

2.1. SnO_2/Graphene Synthesis. GNSs were synthesized using a modified Hummers method followed by the rapid heating of graphene oxide at 1050 °C for 30 s under Ar atmosphere.[22] SnO_2/graphene composites were synthesized by a rapid MWHM method. In a typical process, 22.5 mg of $SnCl_2·2H_2O$ was dissolved in 10 mL of water. Then, 8.25 mg of the as-prepared GNSs was added in the solution followed by vigorous ultrasonication for 2 h. The resulting black suspension was transferred and sealed in a high pressure Teflon vessel. These vessels were anchored to a rotor, which was placed on a turntable in a microwave reaction system (Anton Paar Synthos 3000). The turntable was kept spun to ensure uniform heating during the reaction. The power was set at 1200 W with 8 min ramping time to reach 200 °C, and maintained at this temperature for 1 h before the system was cooled down to room temperature, and the SnO_2/graphene nanocomposites were collected. The pressure was below 20 bar throughout the

synthesis. The as-synthesized product was first washed with ethanol and water several times to remove the Cl$^-$ by centrifugation, and followed by vacuum drying in an oven at 80 °C overnight. Pure SnO_2 nanoparticles were prepared under the same parameters except the addition of GNSs. A schematic of the synthesis process is depicted in Scheme 1.

2.2. Characterization. Powder X-ray diffraction (XRD, Rigaku RU-200BVH with a Co-Kα source (λ = 1.7892 Å)) was used to analyze the phase composition of the as-prepared SnO_2/graphene sample. Raman microspectroscopy (HORIBA Scientific LabRAM HR Raman spectrometer) was conducted under ambient conditions with an incident laser beam at 532.03 nm. The SnO_2 contents (wt %) in the composites were determined by thermogravimetric analysis (TGA; Netzsch) with a heating rate of 10 °C min^{-1} in air from room temperature to 900 °C. Field emission scanning electron spectrometry (FE-SEM, Hitachi 4800S) coupled with energy dispersive spectroscopy (EDS), transmission electron microscope (TEM, Hitachi H-7000), and high-resolution TEM (HRTEM, JEOL 2010 FEG microscope) were used to characterize the microscopic features. The XANES experiments on the Sn $M_{5,4}$ edge, O K edge, and C K edge were conducted on the undulator Spherical Grating Monochromator (SGM) beamline at the Canadian Light Source (CLS) located at the University of Saskatchewan in Saskatoon. XANES were recorded in total electron yield (TEY) using specimen current and X-ray fluorescence yield (FLY) using a multichannel plate.[23]

2.3. Electrochemical Measurement. To evaluate the electrochemical performance of the composites, the samples were mixed with conductive carbon black and polyvinylidene fluoride in a weight ratio of 80:10:10 in N-methylpyrrolidinone (NMP) solvent. Then, the slurry was uniformly cast on a copper foil (loading of SnO_2/graphene is 0.67 mg/cm^2) and dried at 70 °C under vacuum overnight. The coin cells were assembled inside an argon-filled glovebox using lithium metal foil as the counter electrode and the polypropylene as the separator. The electrolyte was 1 M LiPF$_6$ dissolved in ethylene carbonate (EC) and dimethyl carbonate (DMC) solvent (1:1 volume ratio). The cells were tested on a computer controlled battery tester system (Arbin BT-2000). The profiles of galvanostatically charging and discharging curves were obtained at a voltage range of 0.01 to 3 V (vs Li$^+$/Li) at a current density of 60 mA g^{-1}. Cyclic voltammetry (CV) measurements were performed on an electrochemical workstation (Potentiostat/Galvanostat/EIS (VMP3)) over the potential range of 0.01−3.0 V (vs Li$^+$/Li) at a scanning rate of 0.1 mV s^{-1}. Electrochemical impedance spectroscopy (EIS) measurements were conducted by applying an AC voltage of 5 mV amplitude in the frequency range from 0.01 to 100 kHz at 0.7 V of the 10th discharge cycle.
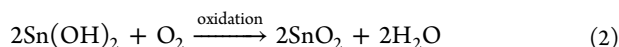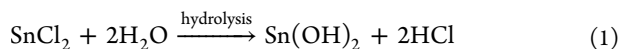
3. RESULTS AND DISCUSSION

Scheme 1 presents the fabrication process of SnO_2/graphene composites. With this advanced MAHM technique, hybrid SnO_2/graphene nanocomposites were obtained within only one hour. Tin(II) chloride underwent rapid hydrolysis with the assistance of microwave heating and were transformed to $Sn(OH)_2$, which were then quickly oxidized to SnO_2 by the residue oxygen in the Teflon vessels at 200 °C. Meanwhile, the fast reaction rate effectively inhibited possible aggregation of SnO_2 nanoparticles and the stacking of GNSs. A possible mechanism for the reaction was described in the following equations:
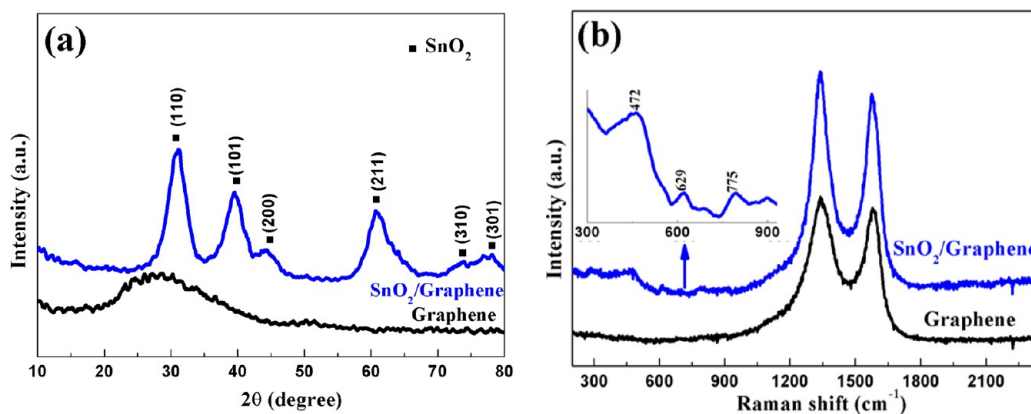
Figure 1. Characterization of graphene and as-prepared SnO_2/graphene nanocomposites: (a) XRD and (b) Raman spectra.
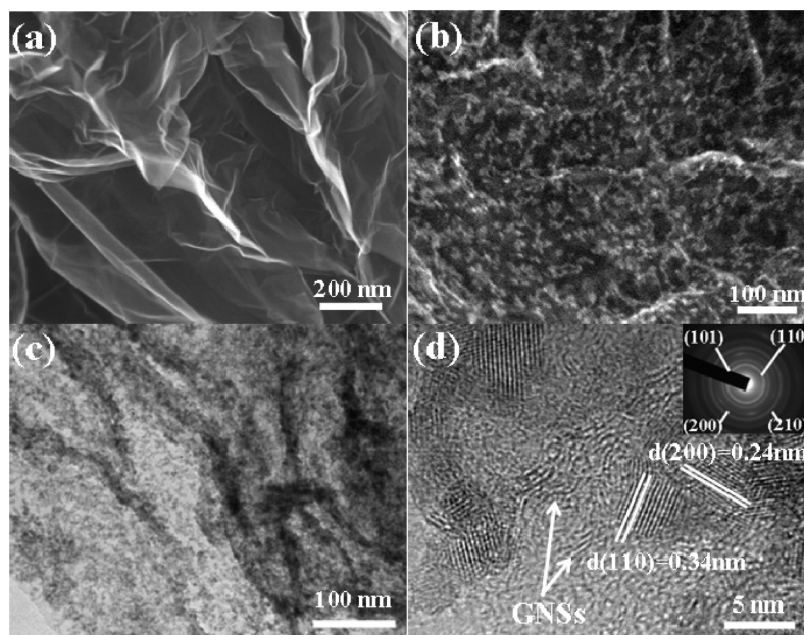
Figure 2. SEM images of (a) GNSs and (b) SnO_2/graphene nanocomposites; (c) TEM image and (d) HRTEM image of SnO_2/graphene nanocomposites. The inset in panel d is the SAED pattern.

$$SnCl_2 + 2H_2O \xrightarrow{\text{hydrolysis}} Sn(OH)_2 + 2HCl \qquad (1)$$

$$2Sn(OH)_2 + O_2 \xrightarrow{\text{oxidation}} 2SnO_2 + 2H_2O \qquad (2)$$

The XRD patterns of GNSs and as-prepared SnO_2/graphene nanocomposite are illustrated in Figure 1a. All strong diffraction peaks in Figure 1a (top line) are consistent with tetragonal crystalline SnO_2 (JCPDS No. 41-1445).[4] It is noted that there is no obvious GNSs patterns in the composites,[21] due to the overlap of the diffraction peak for graphene (002) facet with that of (110) facet for SnO_2 and also the relatively weak intensity (bottom line) compared with SnO_2. The broad diffraction patterns indicate small particle size of the deposited SnO_2. On the basis of the (101) peak of SnO_2, the average crystal size is around 3.5 nm according to Scherrer's equation.

The SnO_2/graphene composite was examined by Raman spectroscopy in comparison to GNSs. As shown in Figure 1b, the peaks at 1340 and 1582 cm^{-1} are both observed, which stand for the D-band and the G-band, respectively.[24,25] It is noteworthy that the intensity ratio of I_D/I_G for the SnO_2/graphene composites is almost the same as GNSs, indicating no

modification in the average size of the sp^2 graphitic domains in the composites. Thus, SnO_2 nanocrystals did not change the pristine laminated structure of GNSs. For the SnO_2/graphene composites, it shows three visible Raman peaks at 472, 633, and 775 cm^{-1}, corresponding to the E_g, A_{1g}, and B_{2g} vibration modes of the rutile SnO_2 structure, respectively.[26]

The typical top view SEM image of GNSs is presented in Figure 2a. Obviously, the layered platelets composed of curled nanosheets are displayed, which are representative structure of GNSs. FE-SEM and TEM have been employed to unveil the morphology of the composites. It is also apparent from Figure 2b that the GNSs are uniformly covered by the ultrafine SnO_2 nanoparticles, which can be confirmed by TEM images (Figure 2c). Dark field TEM image of SnO_2/graphene composites (Figure S1, Supporting Information) also reveals the homogeneous distribution of SnO_2 nanoparticles. A closer examination of the nanocomposites shown in Figure 2d confirms that the average size of highly dispersed SnO_2 nanoparticles is around 3.47 nm, close to the value calculated from the XRD pattern (3.50 nm); moreover, the HRTEM images display two distinguishable images, linear strips of GNSs
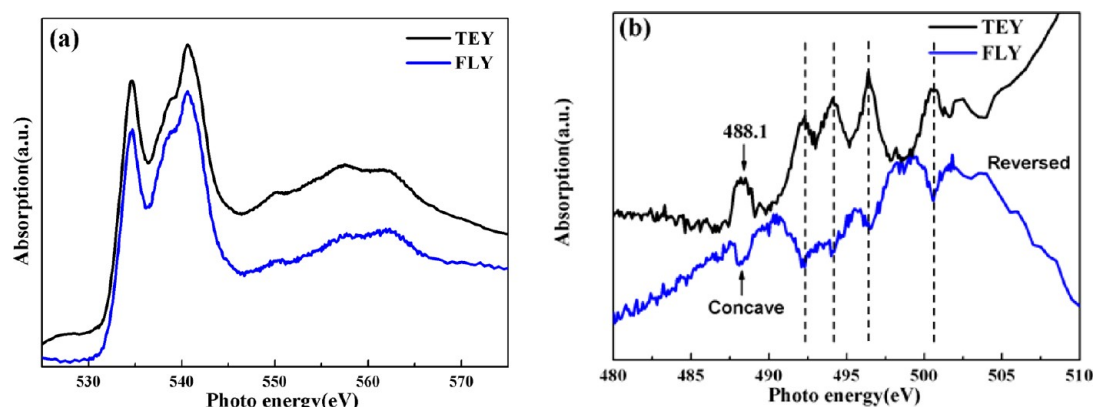
Figure 3. XANES region of the XAS spectra of the SnO$_2$/graphene composites: (a) O K edge and (b) Sn M$_{5,4}$ edge, the FLY is inverted due to self-absorption.

and spherical SnO$_2$ nanoparticles. The d-spacing of GNSs is estimated to be about 0.38 nm, which is much larger than that of the pristine graphite (0.34 nm), while the interplanar distances of 0.34 and 0.24 nm can be identified as $d(110)$ and $d(200)$ of SnO$_2$ nanoparticles, respectively. According to the selected area electron diffraction (SAED) pattern (inset of Figure 2d), four distinct diffraction rings stand for the (110), (101), (200), and (210) crystalline planes of SnO$_2$, confirming the highly crystalline feature of SnO$_2$ nanoparticles. The crystalline feature for SnO$_2$ nanoparticle could also be clearly seen from the high angle annular dark field scanning transmission electron microscopy images (Figure S2, Supporting Information). Such nanocomposites based on the three dimensional (3D) GNSs electronic conductive network have good electronic conductivity and can better facilitate the immersion of electrolyte due to the considerable surface area. Also, it is worthy to mention that the widespread dispersed SnO$_2$ nanoparticles on GNSs could make full use of the GNSs as an excellent matrix to buffer the volume change of the Sn lattice during cycling. All these advantages in structure could contribute to improve the battery performance of SnO$_2$ anode for LIBs.

In order to define the SnO$_2$ contents (wt %) in the as-prepared SnO$_2$/graphene composite, TGA was performed in the temperature range from room temperature to 900 °C in air. GNSs in the SnO$_2$/graphene nanocomposites are oxidized to CO$_2$ from 200 to 600 °C with a corresponding weight loss of 37% (as shown in Figure S3, Supporting Information). Thus, the content of SnO$_2$ in the nanocomposites is 63%. According to the amount of starting precursor SnCl$_2$ and GNSs, the designated weight percentage for SnO$_2$ in the composites is 64.5%. Thus, the conversion of the SnCl$_2$ is nearly 98%, illustrating high efficiency and controlled composition design of the microwave-assisted hydrothermal system.

Exploring how SnO$_2$ nanoparticles are immobilized on the GNSs is very helpful to understand the hybrid structure for achieving the enhanced performance. Here, we investigated the unusual electronic properties of nanosized SnO$_2$, especially after its application to the hybrid structure with GNSs by XANES, which is very sensitive to the local chemical environment of the element.

Figure 3 shows the O K edge and the Sn M$_{5,4}$ edge XANES spectra for SnO$_2$/graphene measured in total electron yield (TEY) and fluorescence yield (FLY) modes. These spectra track the unoccupied densities of states (DOS) of the atom of interest in the composite via dipole transitions. Thus, the O K and Sn M$_{5,4}$ edge tracks the unoccupied DOS of O and Sn p character, respectively. In addition, TEY and FLY provide surface and bulk sensitivity. From the O K edge XANES (Figure 3a), the FLY spectrum tracks that of TEY, i.e., all exhibit positive edge jump with no noticeable broadening in the FLY. This observation indicates that the sample is sufficiently thin compared with the absorption cross-section at the O K-edge. It should be noted that, for a small edge jump relative to the pre-edge absorption, FLY often suffers a thickness effect (self-absorption), resulting in noticeable broadening and even an inversion (see Sn M$_{5,4}$ edge discussion below). These spectral features arise from O 1s to 2p transition, probing the unoccupied densities of state of O 2p character in the conduction band. The Sn M$_{5,4}$ edge XANES (Figure 3b) corresponds to electron transitions from Sn 3d to the conduction band of Sn 5p character. Two sets of triplet peaks beginning at ~490 and 498 eV were observed, corresponding to 3d$_{5/2}$ and 3d$_{3/2}$ to 5p$_{3/2}$ and 5p$_{3/2,1/2}$ transitions, respectively. These are characteristic of rutile SnO$_2$ nanostructure features, in good agreement with previous results.[27] The Sn M$_{5,4}$ edge tracked by the two yields (TEY and FLY) are, however, dissimilar; in fact, FLY is inverted due to self-absorption. As noted above, inversion can occur in FLY in soft X-ray spectroscopy when the sample is thick relative to the penetration depth (often described as the 1/e or one-absorption length of the specimen), and the edge jump is very small relative to the absorption below the edge. A simple calculation using the X-ray calculator shows that, for SnO$_2$, the Sn M$_{5,4}$ edge jump, $(\mu_{\text{above}} - \mu_{\text{below}})/\mu_{\text{below}}$, is ~4%, while the O K edge jump is a factor of ~10.

Returning to the TEY spectrum of the Sn M$_{5,4}$ edge, we clearly see a pre-edge resonance at 488.1 eV just below the Sn M$_5$ edge, which is absent in bulk SnO$_2$. This peak has been previously attributed to surface or defects states caused by unsaturated coordination of surface Sn ions due to oxygen vacancies.[28] In the FLY spectrum, which is bulk sensitive, a small concave (opposite of bump) also appeared at 488.1 eV, demonstrating that the whole specimen containing SnO$_2$ nanoparticles is rich in surface or defects states due to their small size[29] and large surface to volume ratio. Such abundant surface states will likely facilitate charge redistribution and transport between SnO$_2$ and GNSs.

In order to further clarify the interaction, carbon K edge XANES was also performed on SnO$_2$/graphene composites and
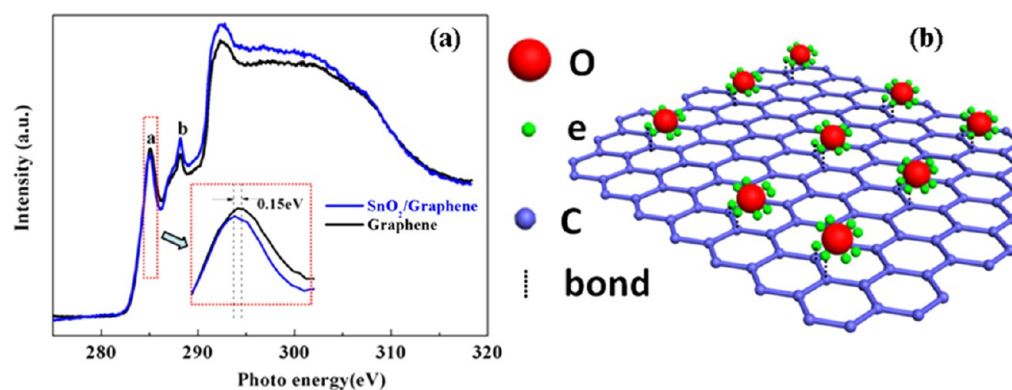
Figure 4. (a) Carbon K edge XANES spectra of the SnO$_2$/graphene composites and graphene. The inset indicates the energy shift. (b) Schematic of the interaction between GNSs and nanoparticles.
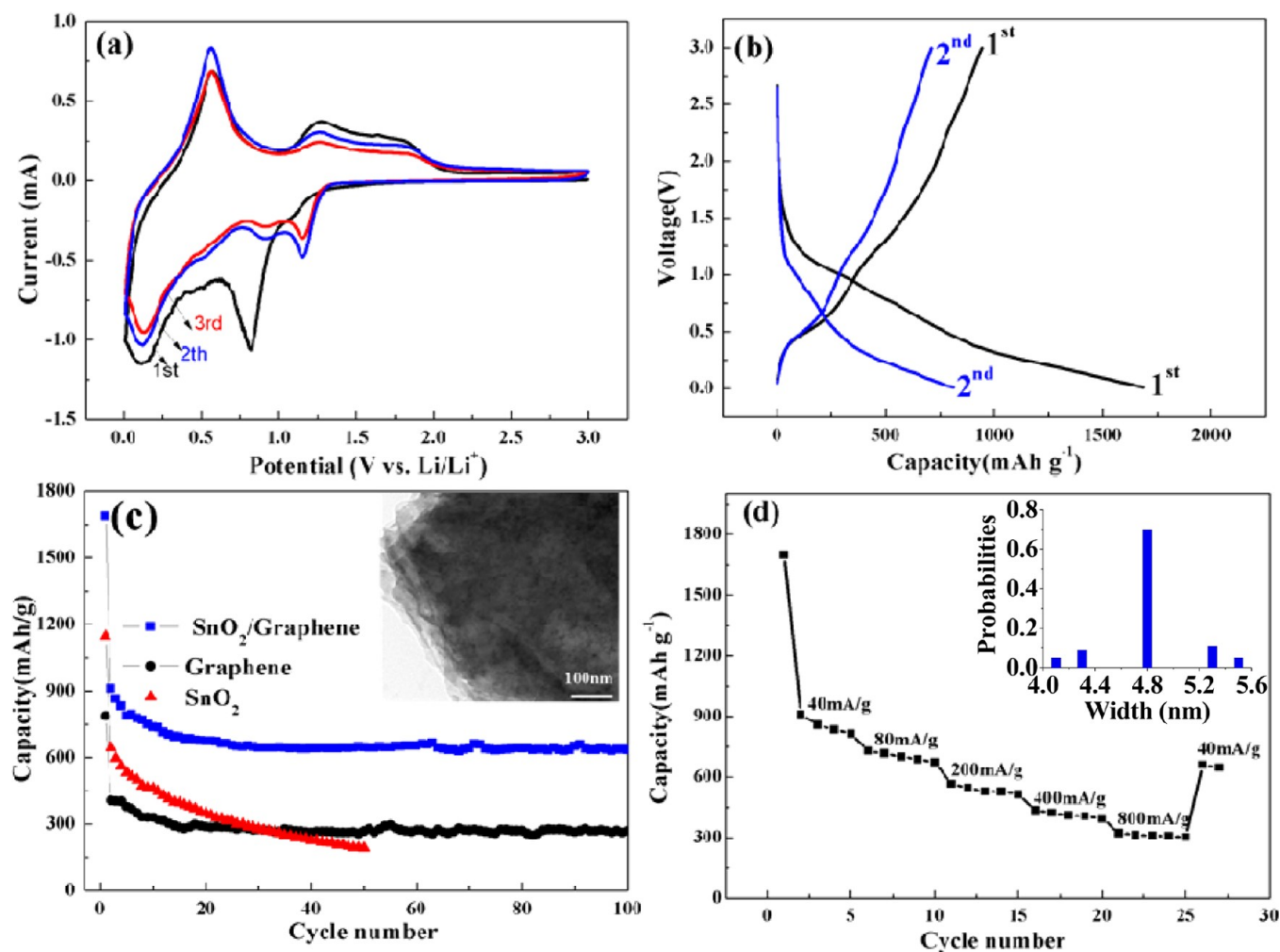
Figure 5. Electrochemical performance of SnO$_2$/graphene composites. (a) Cyclic Voltammetry (CV). (b) First two charge−discharge profiles. (c) Cycle performance plots of bare graphene, SnO$_2$, and SnO$_2$/graphene composites at 60 mA g^{-1}; inserted TEM image shows the morphology of nanocomposite electrodes after cycling. (d) Rate performance, and inset shows size distribution of nanoparticles in composites after cycling.

compared with pure GNSs in TEY mode, as shown in Figure 4. Similar graphitic π^* transition and σ^* transition at 291.5 and 292.5 eV could also be tracked for SnO$_2$/graphene composites, indicating that graphene still keeps the graphitic framework intact after hybridization with SnO$_2$. The broad peak b centered at 288.3 eV reflects the resonance from the carboxylic group, a chemical defect often found in graphitic systems such as

nanotube and graphene.[30] More intriguingly, following interesting features unveiled the interaction between SnO$_2$ and GNSs: First, for peak a (π^* transition, which is proportional to unoccupied density of states), the intensity decreased after SnO$_2$ deposited on GNSs compared with pure GNSs, illustrating that a n-type SnO$_2$ semiconductor donates electrons to 2p-derived π^* states of GNSs. Second, SnO$_2$/

graphene exhibits a more intense resonance for peak b compared with pure GNSs; and the enhanced carboxylate bonding at 288.3 eV should be interpreted as interaction of SnO_2 with GNSs through chemical bonding. Third, as indicated in the inset spectrum, which shows the magnified spectrum of the red square region, it exhibits a slight energy shift of 0.15 eV to lower photon energy for composites compared with that of pure GNSs, consistent with the interpretation that carbon atoms of GNSs accept the electrons donated by SnO_2 nanopaticles. This further confirms that charge redistribution indeed takes place between SnO_2 and GNSs. It is conceivable that defect rich SnO_2 nanoparticle play an important role in immobilizing itself onto GNSs via electrostatic or electronic interaction to form a Sn−OO−C bond through the carboxylic functional group. This notion is in good agreement with recent work of SnO_2 nanoparticles on carbon nanotubes.[30] As a result, since SnO_2 is anchored onto GNSs intimately through spectroscopic evidence, enhanced electrochemical performance could be expected. A schematic for illustrating the chemical bonding and charge redistribution between nanoparticles and graphene is shown in Figure 4b.

To evaluate the electrochemical reactivity of the SnO_2/graphene composites, cyclic voltammetry was performed, as shown in Figure 5a. In the first cycle, two obvious peaks appeared in the cathodic process, located around 0.8 and 0.12 V, respectively. The peak at around 0.8 V is attributed to the reduction of SnO_2 to Sn, the synchronous product of Li_2O (eq 3) and the formation of solid electrolyte interphase (SEI) layer.[29] The peak at 0.12 V occurs from the formation of a series of Li_xSn alloys (eq 4). In the anodic process, two oxidation peaks around 0.12 and 0.57 V stand for the lithium extraction from the GNSs (eq 5) and dealloying of the Li_xSn (eq 4), respectively. It is interesting to note that one distinguished oxidation peak at 1.27 V shows up, demonstrating that eq 3 is partially reversible,[31−34] resulting in the decomposition of Li_2O. Accordingly, the reduction peaks at 1.15 V in the second and third cycles are attributed to the formation of Li_2O again.[9]

$$SnO_2 + 4Li^+ + 4e^- \rightarrow 2Li_2O + Sn \tag{3}$$

$$Sn + xLi^+ + xe^- \leftrightarrow Li_xSn \quad (0 \leqslant x \leqslant 4.4) \tag{4}$$

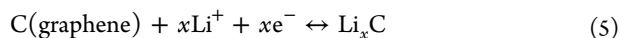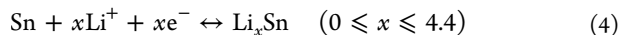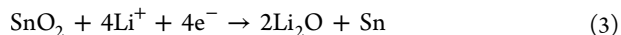$$C(graphene) + xLi^+ + xe^- \leftrightarrow Li_xC \tag{5}$$

Figure 5b presents the charge and discharge profiles of the composites at a current density of 60 mA g^{-1} with a voltage range of 0.01−3 V. The initial small plateau in the potential range of 1.2 to 0.8 V stands for a classical conversion reaction between SnO_2 and Li$^+$, resulting in the formation of Sn and Li_2O in the first discharge process. This is in accordance with the cathodic peak at around 0.8 V in the CV curves. The following long slope profiles of SnO_2/graphene nanocomposites indicated the formation of Li−Sn alloys and Li$^+$ intercalation into GNSs. The plateau (from 1.2 to 0.8 V) almost disappears at the second cycle, demonstrating that major Li_2O is formed in the first cycle. Because of this irreversible reaction, as well as the SEI formed on the anodes,[4] the discharge capacity dropped from 1688 mAh g^{-1} to 911 mAh g^{-1} in the first two cycles.

Cyclic performance of the SnO_2/graphene nanocomposite is illustrated in Figure 5c in comparison with that of the pure GNS anode. GNSs delivered a specific capacity of 784 mAh g^{-1} in the first discharge and exhibited an obvious fading at the

second cycle, retaining only 270 mAh g^{-1} in the 100th cycle. As we mentioned in the introduction section, the SnO_2 anode with high capacity has an obvious disadvantage of the large volume change upon repeating cycling. As a result, the pure SnO_2 nanoparticles result in very low capacity retention that it can reach a reversible capacity of only 191 mAh g^{-1} in the 50th cycle. Refer to the composites, the initial reversible discharge capacity is 911 mAh g^{-1}. As the result of the anchoring of the SnO_2 nanoparticles on the matrix of GNSs in the nanocomposite, the cycle performance has been greatly improved, and the capacity remains almost constant after the 15th cycle. At the 100th cycle, the discharge capacity still remains 635 mAh g^{-1}, which is about 70% retention of the reversible capacity. The coulombic efficiency of SnO_2/graphene (as shown in Figure S4, Supporting Information) in the first cycle is around 44% and then keeps increasing. It is over 95% after 12 cycles and maintains a high Coulombic efficiency of more than 99% in further cycles. It is well-known that SnO_2 anode suffers the huge volume change during cycling, resulting in rapid capacity fading.[4,5] Here, the minimized aggregation of GNSs is due to the jamming of spatially separating SnO_2 nanoparticles, hence, 3D confinement of SnO_2 nanoparticles by GNSs are beneficial for achieving better cycling performance. Besides, the SnO_2 nanoparticles and the elastic GNSs in the hybrid SnO_2/graphene nanocomposites not only help release the stress formed during the lithium insertion process but also decrease the pulverization. Clearly, the GNSs as a good matrix can provide the important function in buffering volume change of SnO_2 anode, thereby enhancing its cycling stability.

The TEM image in the inset of Figure 5c shows the morphology of the nanocomposite electrode after 100 cycles at 60 mA g^{-1}. It reveals that the fine Sn nanoparticles remained highly dispersive in the GNSs matrix without any obvious volume change. The average size of nanopariticles is around 4.8 nm (the inset of Figure 5d), which is very close to that of initial particle size, indicating no obvious aggregation during cycling. This observation indicates that Sn nanoparticles are tightly pinned onto the GNSs and that the detrimental agglomeration of nanoparticles was effectively alleviated to a large extent. More importantly, it is evident that dimensionally flexible GNSs can effectively accommodate the Sn volume change and inhibit the pulverization of Sn, thus maintaining the integrity of the whole electrodes.

Figure 5d shows the rate capability of the nanocomposites from a current density of 40 up to 800 mA g^{-1}. The SnO_2/graphene nanocomposite displays an excellent rate capability. The SnO_2/graphene nanocomposite is still capable of delivering a substantial capacity of 717, 566, and 435 mAh g^{-1} at the high current densities of 80, 200, and 400 mA g^{-1}, respectively. Even when the highest current density of 800 mA g^{-1} was applied, the composites still exhibited a high reversible capacity of 330 mAh g^{-1}. It should be noted that, when the current rate was reversed back to low current after 25 cycles, the specific discharge capacity of 711 mAh g^{-1} could be obtained, indicating that 73% of the initial reversible capacity (971 mAh g^{-1}) was recovered again. This result clearly demonstrates that the SnO_2/graphene nanocomposites could tolerate varied discharge current densities, which is a desirable characteristic for high power application. It thus appears that 3D GNSs would work as a highly conductive matrix when anchored by highly dispersed SnO_2 nanoparticles. Also, the ultrafine SnO_2 nanoparticles can shorten the transport path for

both lithium ions and electrons, thus realizing the high rate capability.

Figure 6 shows the electrochemical impedance spectroscopy for pure SnO_2 and $SnO_2/GNSs$ electrodes, performed at 0.7 V
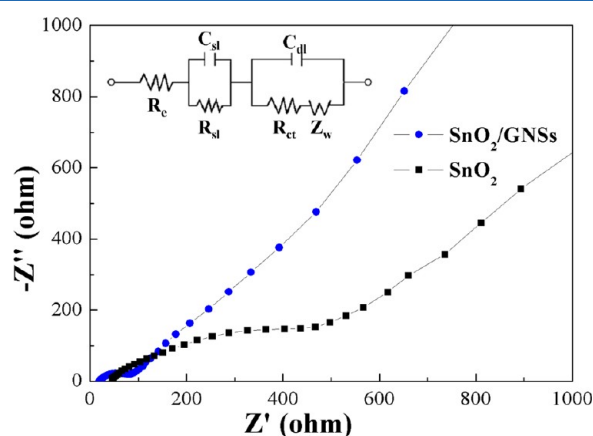
Figure 6. Electrochemical impedance spectra of (a) SnO_2 and (b) $SnO_2/GNSs$. Inset: the equivalent circuit to fit the EIS.

in the 10th discharge cycle. A possible equivalent circuit is given in the inset of Figure 6 for interpretation. R_e denotes electrolyte ohmic resistance, while R_{sl} is the resistance for Li^+ migration through the SEI film; C_{dl} and C_{sl} represent the double layer capacitance and passivation film capacitance, respectively. Z_w is the finite length Warburg impedance, and R_{ct} stands for the charge transfer resistance.[31] The values of R_e, R_{sl}, and R_{ct} are obtained from the simulated data of EIS in Figure 6. It can be clearly seen that the diameter of the semicircle for $SnO_2/GNSs$ is much smaller than that for pure SnO_2, indicating that the impedance value of SnO_2 nanoparticle is higher than $SnO_2/GNSs$ nanocomposites. After simulation by the equivalent circuit, it is found that R_{ct} of SnO_2 and $SnO_2/GNSs$ is 479.31 and 51.93 Ω, respectively. The decreased resistance indicates the enhanced ionic conductivity in the composite, which is beneficial for Li^+ insertion/extraction into the anodes. By fine-tuning the discharge and charge profiles, the $SnO_2/graphene$ nanocomposites are expected to be promising candidates for high-performance anode materials for LIBs.

4. CONCLUSIONS

In summary, 3D $SnO_2/graphene$ nanocomposites were successfully synthesized by a rapid and facile MAHM method. Spatially separated SnO_2 nanoparticles were uniformly loaded on GNSs with content as high as 63 wt %. The electronic structure of the small rutile SnO_2 nanoparticles ($\sim$3.5 nm) have been investigated by XANES, showing that the SnO_2 nanoparticles dispersed on GNSs are abundant of surface and defects states, facilitating the immobilization of the SnO_2 onto GNSs. Carbon K edge XANES features further identify strong interaction (e.g., chemical bonding and charge redistribution) between SnO_2 and GNSs. The resulting $SnO_2/graphene$ composites exhibit a high reversible lithium storage capacity of 653 mAh g^{-1} in the 100th cycle at 60 mA g^{-1}. Furthermore, the nanocomposites can still maintain the discharge capacity as high as 313 mAh g^{-1}, even cycled at high current density as high as 800 mA g^{-1}. Such outstanding performance demonstrates that the $SnO_2/graphene$ nanocomposite systems reported here can be potential anodes for LIB in EV and HEV applications. Also, this work could open a new pathway for

identifying interactions happening in nanocomposite electrodes for LIB by XANES.

■ ASSOCIATED CONTENT

ⓢ Supporting Information
Dark field TEM image, STEM HAADF images, TGA curve, and Coulombic efficiency of $SnO_2/graphene$ composites. This material is available free of charge via the Internet at http://pubs.acs.org.

■ AUTHOR INFORMATION

Corresponding Author
*E-mail: tsham@uwo.ca (T.K.S.); xsun@eng.uwo.ca (X.S.).
Notes
The authors declare no competing financial interest.

■ ACKNOWLEDGMENTS

■ REFERENCES

(1) Cheng, B.; Russell, J. M.; Shi, W. S.; Zhang, L.; Samulski, E. T. *J. Am. Chem. Soc.* **2004**, *126*, 5972−5973.
(2) Dai, Z. R.; Pan, Z. W.; Wang, Z. L. *Adv. Funct. Mater.* **2003**, *13*, 9−24.
(3) Zhang, D. F.; Sun, L. D.; Jia, C. J.; Yan, Z. G.; You, L. P.; Yan, C. H. *J. Am. Chem. Soc.* **2005**, *127*, 13492−13493.
(4) Paek, S. M.; Yoo, E. J.; Honma, I. *Nano Lett.* **2009**, *9*, 72−75.
(5) Idota, Y.; Kubota, T.; Matsufuji, A.; Maekawa, Y.; Miyasaka, T. *Science* **1997**, *276*, 1395−1397.
(6) Lou, X. W.; Li, C. M.; Archer, L. A. *Adv. Mater.* **2009**, *21*, 2536−2539.
(7) Park, M. S.; Wang, G. X.; Kang, Y. M.; Wexler, D.; Dou, S. X.; Liu, H. K. *Angew. Chem., Int. Ed.* **2007**, *46*, 750−753.
(8) Liu, J.; Li, Y.; Huang, X.; Ding, R.; Hu, Y.; Jiang, J.; Liao, L. *J. Mater. Chem.* **2009**, *19*, 1859−1864.
(9) Han, S.; Jang, B.; Kim, T.; Oh, S. M.; Hyeon, T. *Adv. Funct. Mater.* **2005**, *15*, 1845−1850.
(10) Wen, Z.; Wang, Q.; Zhang, Q.; Li, J. *Adv. Funct. Mater.* **2007**, *17*, 2772−2778.
(11) Zhang, H. X.; Feng, C.; Zhai, Y. C.; Jiang, K. L.; Li, Q. Q.; Fan, S. S. *Adv. Mater.* **2009**, *21*, 2299−2304.
(12) Wang, Y.; Lee, J. Y. *J. Power Sources* **2005**, *144*, 220−225.
(13) Yuan, L.; Konstantinov, K.; Wang, G. X.; Liu, H. K.; Dou, S. X. *J. Power Sources* **2005**, *146*, 180−184.
(14) Novoselov, K. S.; Geim, A. K.; Morozov, S. V.; Jiang, D.; Zhang, Y.; Dubonons, S. V.; Grigorieva, I. V.; Firsov, A. A. *Science* **2004**, *306*, 666−669.
(15) Novoselov, K. S.; Geim, A. K.; Morozov, S. V.; Jiang, D.; Katsnelson, M. I.; Grigorieva, I. V.; Dubonons, S. V.; Firsov, A. A. *Nature* **2005**, *438*, 197−200.
(16) Berger, C.; Song, Z. M.; Li, X. B.; Wu, X. S.; Brown, N.; Naud, C.; Mayou, D.; Li, T. B.; Hass, J.; Marchenkov, A. N.; et al. *Science* **2006**, *312*, 1191−1196.
(17) Li, X.; Meng, X.; Liu, J.; Geng, D.; Zhang, Y.; Banis, M.; Li, Y.; Li, R.; Sun, X.; Cai, M.; et al. *Adv. Funct. Mater.* **2012**, *22*, 1647−1654.
(18) Li, F. H.; Song, J. F.; Yang, H. F.; Gan, S. Y.; Zhang, Q. X.; Han, D. X.; Ivaska, A.; Niu, L. *Nanotechnology* **2009**, *20*, 455602.

(19) Yao, J.; Shen, X. P.; Wang, B.; Liu, H. K.; Wang, G. X. *Electrochem. Commun.* **2009**, *11*, 1849−1852.

(20) Zhang, M.; Lei, D. N.; Du, Z. F.; Yin, X. M.; Chen, L. B.; Li, Q. H.; Wang, Y. G.; Wang, T. H. *J. Mater. Chem.* **2011**, *21*, 1673−1676.

(21) Lian, P. C.; Zhu, X. F.; Liang, S. Z.; Li, Z.; Yang, W. S.; Wang, H. H. *Electrochem. Acta* **2011**, *56*, 4532−4539.

(22) Hummers, W. S.; Offeman, R. E. *J. Am. Chem. Soc.* **1958**, *80*, 1339.

(23) Regier, T.; Paulsen, J.; Wright, G.; Coulthard, I.; Tan, K.; Sham, T. K.; Blyth, R. I. R. *AIP Conf. Proc.* **2007**, *879*, 473−476.

(24) Tuinstra, F.; Koenig, J. L. *J. Chem. Phys.* **1970**, *53*, 1126−1130.

(25) Ferrari, A. C.; Robertson, J. *Phys. Rev. B* **2000**, *61*, 14095−14107.

(26) Peercy, P. S.; Morosin, B. *Phys. Rev. B* **1973**, *7*, 2779−2786.

(27) Zhou, X. T.; Heigl, F.; Murphy, M. W.; Regier, T.; Coulthard, I.; Blyth, R. I. R.; Sham, T. K. *Appl. Phys. Lett.* **2006**, *89*, 213109.

(28) Zhou, X. T.; Zhou, J. G.; Murphy, M. W.; Ko, J. Y. P.; Heigl, F.; Regier, T.; Blyth, R. I. R.; Sham, T. K. *J. Chem. Phys.* **2008**, *128*, 144703.

(29) Kucheyev, S. O.; Baumann, T. F.; Sterne, P. A.; Wang, Y. M.; Van Buuren, T.; Hamaza, A. V.; Terminello, L. J.; Willey, T. M. *Phys. Rev. B* **2005**, *72*, 035404.

(30) Zhou, J. G.; Wang, J.; Fang, H. T.; Sham, T. K. *J. Mater. Chem.* **2011**, *21*, 5944−5949.

(31) Lou, X. W.; Chen, J. S.; Chen, P.; Archer, L. A. *Chem. Mater.* **2009**, *21*, 2868−2874.

(32) Poizot, P.; Laruelle, S.; Grugeon, S.; Dupont, L.; Tarascon, J. M. *Nature* **2000**, *407*, 496−499.

(33) Gao, M.; Chen, X.; Pan, H.; Xiang, L.; Wu, F.; Liu, Y. *Electrochem. Acta* **2010**, *55*, 9067−9074.

(34) Titirici, M. M.; Hu, Y. S.; Demir-Cakan, R.; Maier, J.; Antonietti, M. *Chem. Mater.* **2008**, *20*, 1227−1229.